Biodegradable dendritic positron-emitting nanoprobes for the noninvasive imaging of angiogenesis

Adah Almutairi[a], Raffaella Rossin[b], Monica Shokeen[b], Aviv Hagooly[b], Ashwin Ananth[c], Benjamin Capoccia[c], Steve Guillaudeu[a], Dana Abendschein[c], Carolyn J. Anderson[b], Michael J. Welch[b], and Jean M. J. Fréchet[a,1]

[a]College of Chemistry, University of California, Berkeley, CA 94720-1460; and Departments of [b]Radiology and [c]Internal Medicine and Center for Cardiovascular Research, School of Medicine, Washington University, St. Louis, MO 63110

Contributed by Jean M. J. Fréchet, November 20, 2008 (sent for review July 17, 2008)

A biodegradable positron-emitting dendritic nanoprobe targeted at $\alpha_v\beta_3$ integrin, a biological marker known to modulate angiogenesis, was developed for the noninvasive imaging of angiogenesis. The nanoprobe has a modular multivalent core-shell architecture consisting of a biodegradable heterobifunctional dendritic core chemoselectively functionalized with heterobifunctional polyethylene oxide (PEO) chains that form a protective shell, which imparts biological stealth and dictates the pharmacokinetics. Each of the 8 branches of the dendritic core was functionalized for labeling with radiohalogens. Placement of radioactive moieties at the core was designed to prevent in vivo dehalogenation, a potential problem for radiohalogens in imaging and therapy. Targeting peptides of cyclic arginine–glycine–aspartic acid (RGD) motifs were installed at the terminal ends of the PEO chains to enhance their accessibility to $\alpha_v\beta_3$ integrin receptors. This nanoscale design enabled a 50-fold enhancement of the binding affinity to $\alpha_v\beta_3$ integrin receptors with respect to the monovalent RGD peptide alone, from 10.40 nM to 0.18 nM IC_{50}. Cell-based assays of the ^{125}I-labeled dendritic nanoprobes using $\alpha_v\beta_3$-positive cells showed a 6-fold increase in $\alpha_v\beta_3$ receptor-mediated endocytosis of the targeted nanoprobe compared with the nontargeted nanoprobe, whereas $\alpha_v\beta_3$-negative cells showed no enhancement of cell uptake over time. In vivo biodistribution studies of ^{76}Br-labeled dendritic nanoprobes showed excellent bioavailability for the targeted and nontargeted nanoprobes. In vivo studies in a murine hindlimb ischemia model for angiogenesis revealed high specific accumulation of ^{76}Br-labeled dendritic nanoprobes targeted at $\alpha_v\beta_3$ integrins in angiogenic muscles, allowing highly selective imaging of this critically important process.

dendrimer | molecular imaging

Nanotechnology has the potential to revolutionize the diagnosis and treatment of cardiovascular disorders, mitigating the huge social and economic costs of diseases (1). Diseases are biological processes, and positron emission tomography (PET) is sensitive to and informative of these processes. Angiogenesis, a process involving the formation of new capillaries by cellular outgrowth from existing microvessels, has an important role in many human diseases (2) such as cancer, cardiomyopathy, atherosclerosis, and peripheral arterial disease. In a cardiovascular setting, angiogenesis is triggered by hypoxia and ischemia, and its major consequence in tissues is the restoration of perfusion and oxygenation. Therefore, the goal of proangiogenic therapy in the management of ischemic diseases is to stimulate the growth of new blood vessels to improve tissue function. To this aim, a number of angiogenic factors have been evaluated in clinical trials. However, the lack of a reliable and noninvasive technique to directly assess the presence of angiogenesis has been a major drawback in evaluating the outcomes of these trials (3). Additionally, imaging of angiogenesis would be valuable in risk stratification of patients with arterial occlusive disease (2). Noninvasive strategies to study angiogenesis, among other biological processes, have relied on high-affinity monovalent interactions between a cellular target (surface receptors or intracellular components such as DNA) and a small-molecule probe (2). However, this approach often lacks the selectivity for cells that highly express $\alpha_v\beta_3$ integrin, a biological marker known to modulate angiogenesis, over cells with normal expression of $\alpha_v\beta_3$ integrin (4). Additionally, small-molecular imaging agents have the disadvantage of being either rapidly cleared or metabolized and may not accumulate sufficiently in the target tissue (5). We imagined that a nanoscale imaging probe, with design principles and dimensions borrowed from nature, such as globular dimensions in the 5- to 20-nm region, a core-shell architecture, and multivalent targeting, would posses numerous advantages over current positron emitting imaging agents. Herein, we report a dendritic PET imaging nanoprobe with a radioactive core and a protective shell consisting of polyethylene oxide (PEO) chains appended with multiple peptide ligands to target $\alpha_v\beta_3$ integrin overexpressed in angiogenesis. We show this PET nanoprobe has enhanced bioavailablity, in vivo radiostability, binding, and most importantly, increased specificity for tissue that overexpresses $\alpha_v\beta_3$.

Results and Discussion

Over the last decade, the medical community has made widespread use of synthetic polymeric and dendrimeric nanoparticles to overcome biological barriers and enhance in vivo imaging, drug delivery, gene therapy, and tissue engineering (1). These applications are facilitated by the ability to easily tune the size, chemistry, topology, and ultimately, the properties of polymers through chemical synthesis. Multivalent carriers come in a variety of sizes and architectures, and they can be carefully designed to amplify both signal and targeting of specific diseased tissues. Importantly, nanoprobes such as the one reported herein can be designed to isolate and protect the radioactive moiety from being rapidly recognized and metabolized (6, 7). Moreover, the amplification of binding affinity via multivalent interactions as opposed to monovalent interactions of high-affinity ligands with integrins is more favorable for targeting overexpressed receptors on cells (4, 8) and more closely mimics natural systems of targeting. However, for successful in vivo targeting, high-affinity multivalent ligands must have the ability to reach the intended target at sufficient concentrations and for a sufficient length of time to be detectable in vivo while evading the immune system (9). Rapid excretion, nonspecific binding, metabolism, and delivery barriers all counteract this process and must be overcome.

Author contributions: A. Almutairi, R.R., M.S., D.A., C.J.A., M.J.W., and J.M.J.F. designed research; A. Almutairi, R.R., M.S., A. Ananth, and B.C. performed research; A. Almutairi, R.R., M.S., A.H., B.C., and S.G. contributed new reagents/analytic tools; A. Almutairi, R.R., M.S., A. Ananth, and J.M.J.F. analyzed data; and A. Almutairi and J.M.J.F. wrote the paper.

The authors declare no conflict of interest.

[1]To whom correspondence should be addressed at: College of Chemistry, University of California, 718 Latimer Hall, Berkeley, CA 94720-1460. E-mail: frechet@cchem.berkeley.edu.

This article contains supporting information online at www.pnas.org/cgi/content/full/0811757106/DCSupplemental.

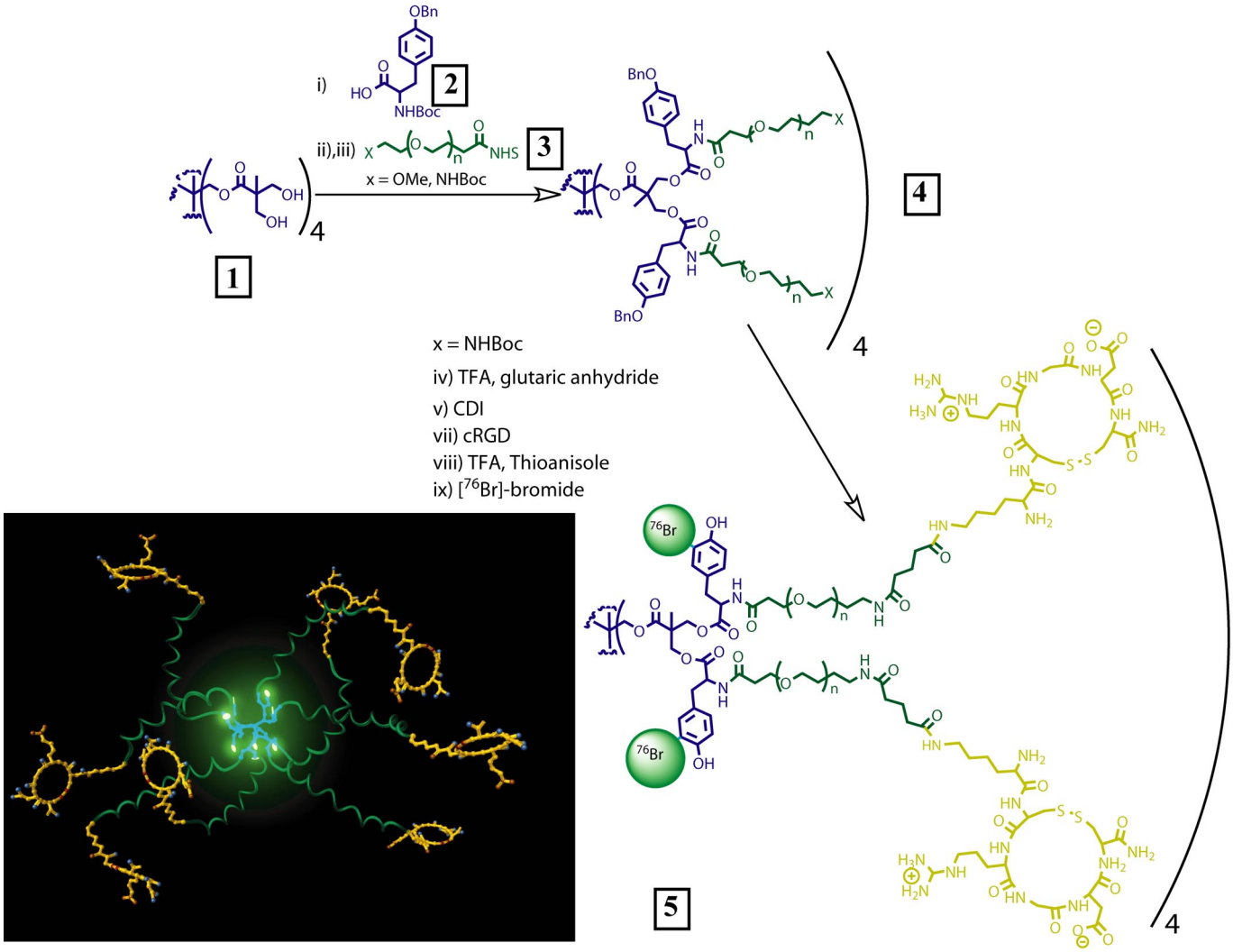

Fig. 1. Preparation of PET nanoprobes targeted at $\alpha_v\beta_3$ integrin.

The properties of dendrimers translate especially well into pharmacology and have led to unprecedented promise in drug delivery and molecular imaging (10). Dendrimers are highly branched macromolecules, with a structural precision approaching that of proteins, and consequently have an increased likelihood of reproducible behavior in patients (11). Furthermore, the multivalent character of dendrimers enables amplification of targeting (8), imaging (10), and therapy (12). Aliphatic polyester dendrimers are well-suited as delivery vehicles because of their biodegradability and biocompatibility (13). Recognition by the reticuloendothelial system, nonspecific tissue accumulation, rapid blood clearance, and destabilization due to harsh and metabolically active media all pose a barrier to the optimal performance of many PET imaging agents (14).

Design and Synthesis of Biodegradable Dendritic PET Nanoprobes. We envisioned a nanoscale carrier with a dendritic core and a flexible multivalent shell. A dendritic core would allow us to exercise control over the size, branching and multivalency of the carrier, which translates into a method to reproducibly modulate the pharmacokinetics of the nanoconstruct. Its circulation half-life can be adjusted from 1.4 ± 0.4 h to 50 ± 10 h by selecting the appropriate level of dendritic branching and length of PEO (7, 15). A modular pharmacokinetic profile is especially beneficial in nuclear medicine, because a large range of radionuclides, with a variety of decay half-lives, used in therapy and diagnosis exists. We functionalized 8 dendritic branches with 8 tyrosine groups to enable attaching radiohalogens, such as ^{122}I, ^{123}I, ^{124}I, ^{125}I, ^{131}I, ^{75}Br, ^{76}Br, and ^{77}Br, useful for imaging and therapy (14). With this approach, the radiolabel is protected at the core with a PEO shell that imparts biological stealth to the particle while allowing for further modulation of the pharmacokinetics. The targeting ligands are attached at the ends of the PEO chains, providing them with sufficient flexibility (16) to bind 2 or more receptors at a time. The cyclic peptide CRGDC was selected to target $\alpha_v\beta_3$ integrin (17) and was modified with lysine to allow tethering the peptide ligands to the nanoprobe. Selection of the generation of the dendritic core, the length of the PEO chains, and the radionuclide depends on the desired pharmacokinetics and the biological process to be studied. The 8 tyrosine residues enable efficient labeling with ^{76}Br or ^{125}I as the radioactive nuclide.

Pentaerythritol was chosen as the dendritic core because it can be divergently dendronized in one step by using a derivative of 2,2-bis(hydroxymethyl) propanoic acid to afford a dendrimer with 8 branching points (Fig. 1). Heterobifunctionality is then introduced by coupling 8 protected tyrosine moieties **2** (Fig. 1) to hydroxylated dendrimer **1**. The amino groups were depro-

tected and 8 heterobifunctional PEO chains **3** (2,700 Da) were attached through an active NHS ester, affording 23,000-Da polymer **4**. Dynamic light-scattering measurements gave a hydrodynamic radius of ≈12 nm for dendrimer **4**. The amine groups at the terminal ends of the heterobifunctional PEO chains were deprotected, coupled to glutaric anhydride, and then converted to active imidazolides. Coupling of these imidazolides to cyclic RGD peptide moieties via a pendant lysine amino group led to an average attachment of ≈5 RGD per dendritic nanoprobe. Finally, the phenolic group of the tyrosine moieties were deprotected with trifluoroacetic acid in the presence of thioanisole and radiolabeled with ^{76}Br. Before systemic administration, we evaluated the stable attachment of the radioactive tag within the nanostructures in PBS and mouse serum and observed <10% dehalogenation (14, 18) after 48 h.

Isolated Integrin Binding and Cell Uptake Studies. The binding affinity of the dendritic nanoprobe toward the target biomarker $\alpha_v\beta_3$ was evaluated in vitro by using a solid-phase (plate-based) heterologous competitive binding assay and a cell-based internalization assay. The $\alpha_v\beta_5$ integrin receptor was also screened, because both $\alpha_v\beta_5$ and $\alpha_v\beta_3$ integrin receptors are expressed on normal tissues and are up-regulated in the course of angiogenesis. The IC_{50} value of the monovalent peptide KCRGDC (in a plate-based isolated integrin assay) is 10.4 nM for $\alpha_v\beta_3$ and 921 nM for $\alpha_v\beta_5$. The IC_{50} value obtained from the plate-based binding assay gave insight into the binding efficiency of the nanoprobe toward its target.

For the targeted dendritic nanoprobe, the IC_{50} value from the $\alpha_v\beta_3$ binding curve was 0.18 nM, and the IC_{50} value for the $\alpha_v\beta_5$ integrin was 10.4 nM. Thus, there was a 50-fold enhancement in the binding of the targeted dendritic nanoprobe to $\alpha_v\beta_3$ and ≈56-fold weaker binding for $\alpha_v\beta_5$ compared with $\alpha_v\beta_3$. The nontargeted dendritic nanoprobe did not bind to either $\alpha_v\beta_3$ or $\alpha_v\beta_5$ integrin.

Cell-based assays were performed to measure the internalization efficiency of the targeted dendritic nanoprobes, by using $\alpha_v\beta_3$-expressing M21 melanoma cells. Corresponding assays were also performed with $\alpha_v\beta_3$-negative M21L cells. The targeted dendritic nanoprobe showed increased internalization over time in the $\alpha_v\beta_3$-positive M21 cells (Fig. 2). There was significantly lower internalization of the targeted dendritic nanoprobe in the presence of block (excess of unlabeled targeted dendritic nanoprobe) and in $\alpha_v\beta_3$-negative M21L cells, consistent with receptor-mediated cell internalization. The nontargeted dendritic nanoprobe did not show significant internalization in either M21 or M21L cells [see supporting information (SI) Fig. S1 for details]. The selectivity for overexpression of $\alpha_v\beta_3$ can be gleaned from the observed difference in cell association of the IC_{50}s ($\alpha_v\beta_3$ vs. $\alpha_v\beta_5$) on the plate-based assay. Additionally, cellular uptake of the targeted probe is higher in $\alpha_v\beta_3$-positive M21 cells versus $\alpha_v\beta_3$-negative M21L (see *SI Text*) cells. Furthermore, in vivo data validated these in vitro results.

In Vivo Biodistribution in Normal Rodents. The effects of size, molecular mass, PEO length, and branching on the biodistribution of polyester dendritic structures have been thoroughly evaluated (7, 12, 13). Blood half-lives ranging from 1.4 ± 0.4 to 50 ± 10 h, depending on branching and PEO length, were reported. The nanostructures exhibited no specific organ accumulation and were cleared efficiently, mainly through the urine and the feces. Previous in vivo studies were carried out at polymer dosage useful for drug delivery and toxicity evaluation (40 mg/kg of body weight and over) (7, 12, 13). In contrast, the amount to be administered for molecular imaging should be kept to a minimum. Accordingly, we compared the in vivo behavior of low doses (≈0.1 mg/kg of body weight) of targeted and nontargeted dendritic nanoprobes in normal rodents. At specific

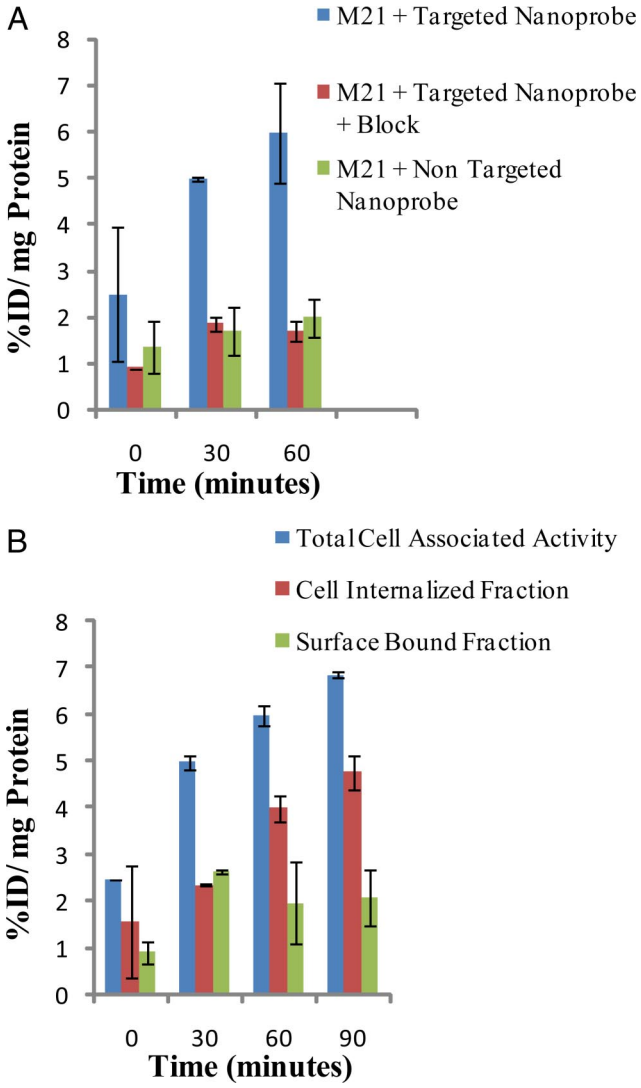

Fig. 2. Cell uptake studies. (*A*) Percentage total cell-associated fraction, cell-internalized fraction, and surface-bound fraction for the targeted nanoprobe in $\alpha_v\beta_3$-positive M21 cells. (*B*) Percentage cell-internalized fraction for the targeted nanoprobe in the absence and presence of the block and the nontargeted nanoprobe in $\alpha_v\beta_3$-positive M21 cells. All values are normalized to the protein content per well. Total cell-associated fraction represents the sum of cell-internalized fraction and surface-bound fraction. %ID/mg Protein refers to percentage injected or administered dose per milligram of protein.

time points after injection (10 min and 1, 4, 24, and 48 h), organs and tissues of interest were removed and blotted dry, and the radioactivity was measured in a γ-counter. We measured the whole stomach including its contents. As expected, the blood retention of the 2 radiolabeled nanoprobes exhibited a very slight but statistically significant difference at most considered time points, except 1 and 48 h after injection (Fig. 3). Slight but significant differences were observed also in other major organs. For instance, we found a slightly higher accumulation of targeted dendritic nanoprobes in organs of the monophagocyte system, such as the liver and spleen, reasonable because of the peripheral RGD functions, which confer molecular recognition but adversely affect immune evasion imparted by the protective PEO shell. Also, higher uptake was observed in the bones at delayed time points. This may be due partly to both accumulation in the bone marrow (part of the monophagocyte system) and in the joints, because of specific interactions with $\alpha_v\beta_3$ integrins overexpressed on osteoclasts (19).

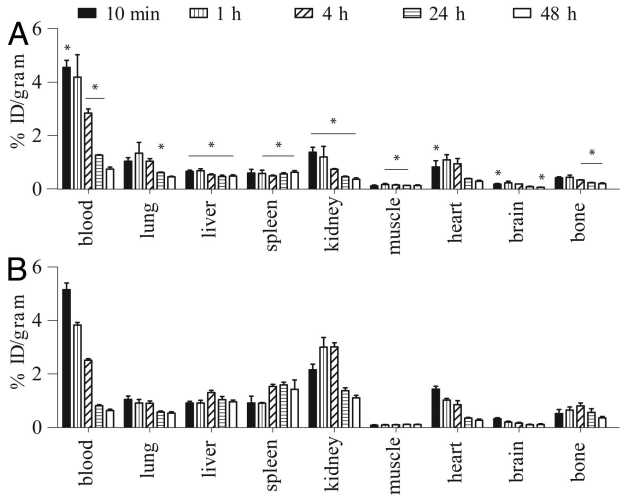

Fig. 3. Biodistribution of nontargeted (*A*) and targeted (*B*) nanoprobes in healthy rats. Bars represent the mean ($n = 4$) percentage injected dose per gram of tissue (%ID/gram) and standard deviations (*, $P < 0.05$ with respect to RGD dendritic nanoprobe).

The largest difference between the 2 nanoprobes, however, was observed in the renal uptake. In fact, the nontargeted dendritic nanoprobe showed the typical uptake and release pattern of rapid urinary elimination, which is fast accumulation in the kidney [1.4 ± 0.2%ID/g at 10 min after injection (p.i.)], followed by an effective release [0.7 ± 0.0%ID/g at 4 h ($P < 0.05$) and 0.3 ± 0.0%ID/g at 48 h p.i.]. However, the renal uptake of targeted dendritic nanoprobe increased from 2.2 ± 0.2%ID/g immediately after administration to ≈3.0%ID/g within a few hours, with incomplete clearance at longer time points (1.1 ± 0.1%ID/g at 48 h p.i.). Most likely, this difference in kidney retention is due to overexpression of $\alpha_v\beta_3$ integrins (20) as well as the difference in charge between the 2 nanostructures, as previously observed for tetrameric vs. monomeric RGD constructs (8). The excretion profile confirms the fast urinary elimination of the nontargeted dendritic nanoprobe (Table 1), whereas apparently no differences in feces radioactivity is observed between the 2 nanoprobes. However, given the fact that at the end of the in vivo evaluation, similar amounts of radioactivity were accounted for with the 2 nanoprobes in the harvested organs (≈40%ID), we expect the RGD dendritic nanoprobe to undergo slow elimination through the intestine (not collected). Importantly, studies using different rodent species showed no difference in nanoprobe biodistribution (*SI Text* and Fig. S2).

The possibility of significant radionuclide release in vivo is unlikely, given the low radioactivity uptake in the brain (Fig. 3) and in the stomach (Table 1). Moreover, chromatographic analysis of plasma samples at various time points indicated no debromination within the first 4 h after nanoprobe administration to the animals and <30% radiobromide release at later time points ($n = 3$). In contrast, previous studies of mice administered ^{76}Br-radiolabeled antibodies noted the complete debromination of the bromotyrosine residues within 24 h p.i. and high stomach uptake of radioactivity as early as 4 h p.i (21). Therefore, as we anticipated during the design of the dendritic nanoprobe, burying the ^{76}Br-tyrosine within the core of the structure, protected by a layer of PEO chains, slows down the in vivo enzymatic dehalogenation. The biodegradable nature of this dendritic core was previously evaluated and is expected to take place over a 2-week time frame (7, 22).

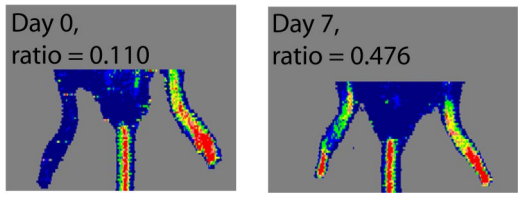

Fig. 4. Laser Doppler perfusion imaging in the hindlimb ischemia model. Images from a representative animal showing the perfusion of the hindlimbs immediately after surgery (Day 0) to induce ischemia of the right leg (shown on the left) and 1 week later. Blue and green areas reflect low levels of perfusion (0–200), whereas yellow, red, and white reflect higher flows (800–1,000). Flow ratios were calculated as the flow in the midthigh in the ischemic leg compared with the flow in the same area in the nonischemic leg. Relative perfusion increased significantly over 1 week after surgery ($P < 0.008$, day 0 vs. day 7).

Hindlimb Ischemia Model in Mice. Animal models of peripheral and myocardial ischemia have facilitated assessment of noninvasive angiogenesis imaging with use of radiolabeled probes targeting vascular growth factors such as $\alpha_v\beta_3$ integrins. The animal model of angiogenesis used in the present study involved ligation of the proximal and distal ends of the femoral artery, followed by excision of the middle portion of the artery and attached side branches (23). This created a unilateral ischemia in the mouse hindlimb, followed by slow revascularization of the ischemic muscle, with a significant increase in capillary density, proliferative activity, and $\alpha_v\beta_3$ expression compared with the nonischemic muscle. This model of hindlimb ischemia, used in a previous study to evaluate the imaging capabilities of a chelate peptide containing the RGD motif, revealed the dependence of probe accumulation on the time after femoral artery ligation (24). A significant but slight increase in probe uptake was observed in the distal part of the ischemic limb between days 3 and 14, with a peak at day 7 after the surgical intervention.

We showed severe hypoperfusion of the right ischemic hindlimb after the double ligation and vascular resection procedure and a significant increase in blood flow (quantified as the ratio of right (ischemic) to left (nonischemic) hindlimb flow) after 7 days, consistent with the restoration of flow induced by angiogenesis (Fig. 4).

PET Imaging of $\alpha_v\beta_3$ in Hindlimb Ischemia Model. PET imaging and post-PET tissue γ-well counting were carried out 24 h after the administration of a dose (≈1 mg/kg of mouse body weight, ≈100

Table 1. Radioactivity excretion and stomach uptake for nontargeted nanoprobe and RGD-nanoprobe

	Nontargeted nanoprobe			RGD-nanoprobe		
Specimen	4 h	24 h	48 h	4 h	24 h	48 h
Stomach†	1.54 ± 0.25	1.77 ± 0.34	1.96 ± 0.28	1.24 ± 0.22	1.65 ± 0.76	2.55 ± 0.40
Urine	8.53 ± 5.68*	24.15 ± 1.58*	31.79 ± 1.78*	2.26 ± 0.64	3.58 ± 0.33	3.95 ± 0.24
Feces	0.00 ± 0.00	0.78 ± 0.57	3.20 ± 0.35	0.02 ± 0.02	2.12 ± 1.04	4.39 ± 1.14

Data represent the mean ($n = 4$) injected dose per organ ± standard deviation (*, $P < 0.05$ with respect to RGD nanoprobe).
†Including stomach contents.

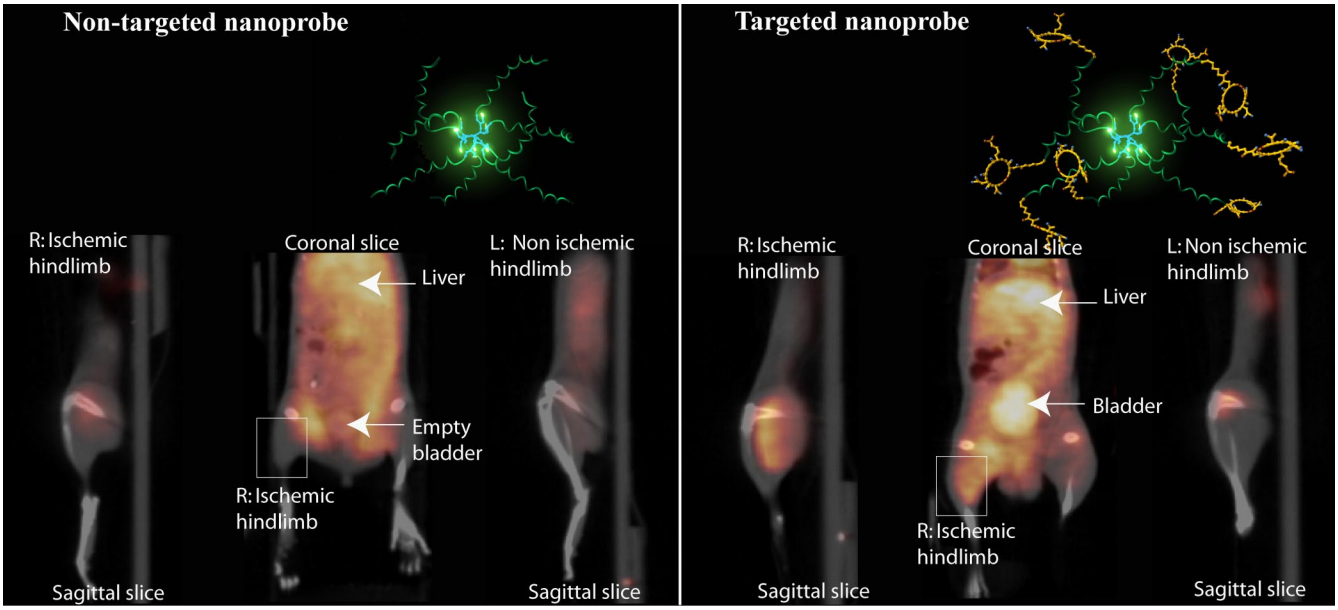

Fig. 5. Noninvasive PET/CT images of angiogenesis induced by hindlimb ischemia in a murine model. (*A*) Nontargeted dendritic nanoprobes (shown bottom center). (*B*) Uptake of $\alpha_v\beta_3$-targeted dendritic nanoprobes was higher in ischemic hindlimb (left side of image) as compared with control hindlimb (right side of image).

μCi per mouse) of either ^{76}Br-labeled targeted dendritic nanoprobe or ^{76}Br-labeled nontargeted dendritic nanoprobe in mice 7 days after the ligation and removal of a segment of the femoral artery in the right hindlimb. The nanoprobe was engineered to circulate in the blood for a prolonged time, thus influencing the time delay to imaging.

Fig. 5 shows representative microPET/CT slices of 2 mice injected with either the nontargeted (*A*) or targeted (*B*) dendritic nanoprobe at 24 h after injection. In both animals, the coronal slices show diffuse radioactivity in the abdominal area, because of urinary (Fig. 5*B*) and hepatobiliary excretion. Remarkably, transaxial and sagittal slices obtained from the mouse injected with RGD-conjugated dendritic nanoprobe show accumulation of radioactivity in the entire thickness of the ischemic muscle, compared with the nonischemic limb (Fig. 5*B*). In contrast, no difference between the 2 limbs is visible in the sagittal slices from the mouse injected with nontargeted dendritic nanoprobe (Fig. 5*A*).

The image- and biodistribution-derived ratios of probe accumulation (ratio of ischemic to nonischemic limb, R/L) for $\alpha_v\beta_3$-targeted vs. nontargeted dendritic nanoprobe in proximal and distal hindlimbs are depicted in Fig. 6.

The R/L image ratio was markedly higher in mice that received the targeted dendritic nanoprobe compared with those injected with the nontargeted dendritic nanoprobe, particularly in the area distal to the excised segment of femoral artery (Fig. 6*A*).

These findings suggest specific interactions between the targeted nanoprobe and $\alpha_v\beta_3$ integrins in angiogenic capillaries. In contrast to previous studies (24), our image analysis showed larger ratios for targeted compared with nontargeted nanoprobes. When the skeletal muscles were excised and the tissue radioactivity measured in a well counter, we found similar results to those obtained by micro PET (Fig. 6*B*) and a strong linear correlation between the methods in all of the mice tested (R^2 = 0.84; Fig. S3). This further substantiates the use of small-animal PET imaging to noninvasively quantify the presence of biological targets, such as those related to angiogenesis, in vivo. Additionally, we observed a slight increase in the ischemic/nonischemic R/L ratio with the nontargeted nanoprobe in the distal hindlimb. This may reflect some nonspecific retention of the nontargeted nanoprobe, perhaps because of interstitial activity associated with changes in vascular permeability or residual blood activity within the hypervascular ischemic hindlimb at 7 days after ischemic injury. Importantly, muscle sections from the ischemic hindlimb showed increased staining for $\alpha_v\beta_3$ receptors compared with the nonischemic hindlimb (Fig. 6*C*).

Conclusion

Noninvasive molecular imaging sets forth not only to probe the molecular abnormalities that are the basis of disease rather than the end result but to directly image noninvasively the effects of therapy in patients. Recently, the effects of size, architecture, and topology of multivalent carriers, in addition to the density of ligands presented, have emerged as decisive factors in their ability to perform as molecular imaging agents. A unique design and a facile synthesis have provided us with a radiohalogen nanoprobe capable of noninvasively imaging angiogenesis. This targeted PET nanoprobe showed a 50-fold enhanced binding affinity to $\alpha_v\beta_3$ integrin receptors, known to modulate angiogenesis, with respect to the monovalent RGD peptide alone. Additionally we found a 6-fold increase in $\alpha_v\beta_3$ receptor-mediated endocytosis of the targeted nanoprobe compared with the nontargeted nanoprobe. In vivo pharmacokinetic studies showed excellent bioavailability for the targeted and nontargeted nanoprobes. In vivo studies in a murine hindlimb ischemia model for angiogenesis revealed high specific accumulation of ^{76}Br-labeled dendritic nanoprobes targeted at $\alpha_v\beta_3$ integrins in angiogenic muscles, allowing highly selective imaging of this critically important process. The modular nature of this nanoprobe allows tuning its blood circulation time, through changes in dendritic branching and PEO length, to suit a variety of radiohalogens used in both imaging and therapy. Thus, we envision this nanoprobe could potentially have implications in both therapy and imaging.

Materials and Methods

Materials were used as obtained from commercial sources. DMF, and DCM, for syntheses were dried before use. The ^{76}Br was produced at the Washington University cyclotron facility by the ^{76}Se(p,n)^{76}Br nuclear reaction on a ^{76}Se-enriched Cu_2Se target. Please see *SI Text* document for synthetic details and characterization data. Cell-internalization assays with ^{125}I-labeled nanoprobes were carried out with M21 and M21L cells. All animal studies were performed in compliance with guidelines set by the Washington University

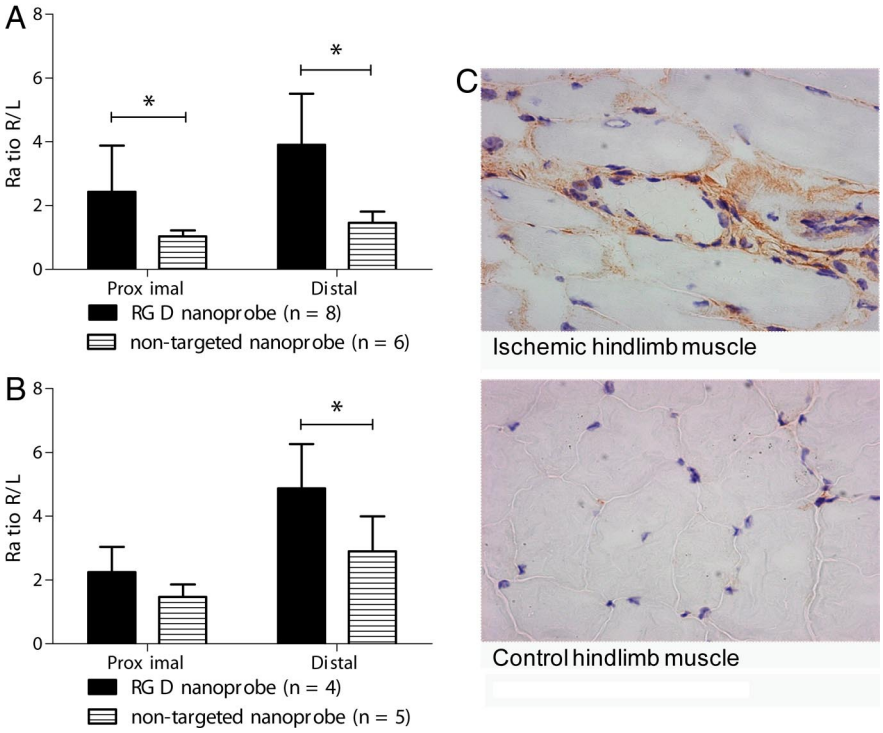

Fig. 6. Ischemic to nonischemic hindlimb (R/L) ratios of targeted and nontargeted nanoprobes and representative photomicrographs of thigh muscle showing $\alpha_v\beta_3$ receptor staining 1 week after induction of hindlimb ischemia. (*A* and *B*) Ischemic to nonischemic hindlimb (R/L) ratios of targeted and nontargeted nanoprobes from imaging analysis (*B*) and γ-well counting of tissues. Bars represent the mean and standard deviation (*, $P < 0.05$). (*C*) Sections from the ischemic hindlimb (*Upper*) showing patches of staining for $\alpha_v\beta_3$ receptors around neovessels and from the contralateral nonischemic hindlimb (*Lower*) showing minimal staining for $\alpha_v\beta_3$ receptors.

Animal Studies Committee. Unilateral hindlimb ischemia was induced in male C57BL/6 mice (8–10 weeks old; The Jackson Laboratory). All procedures were conducted in accordance with the Guide for the Care and Use of Laboratory Animals (U.S. Department of Health, Education, and Welfare publication no. NIH 78-23, 1996) and were approved by the Animal Studies Committee at Washington University. The imaging sessions were carried out by using the MicroPET Focus (Siemens Medical Solutions) and the microCAT II (CTI-Imtek) scanners. MicroPET images (corrected for attenuation, scatter, normalization, and camera dead-time) and microCT images were coregistered by using a landmark registration technique (using fiducial markers directly attached to the animal bed) and AMIRA image display software (TGS). A correction factor was applied (correction factor = calibration factor × scale factor/isotope branching fraction). The image registration between microCT and microPET images was accomplished by using a landmark registration technique with AMIRA image display software (AMIRA; TGS).

ACKNOWLEDGMENTS. A. Almutairi thanks the University of California Office of the President for a postdoctoral fellowship. We thank Dr. Dan Link for use of the laser Doppler unit and Dr. M. Cecilia Giron for statistical analyses. Support from the National Institutes of Health Program of Excellence in Nanotechnology (Grant 1 U01 HL080729-01) is acknowledged with thanks.

1. Couvreur P, Vauthier C (2006) Nanotechnology: Intelligent design to treat complex disease. *Pharmacol Res* 23:1417–1450.
2. Dobrucki LW, Sinusas AJ (2007) Imaging angiogenesis. *Curr Opin Biotechnol* 18:90–96.
3. Sinusas AJ (2004) Imaging of angiogenesis. *J Nucl Cardiol* 11:617–633.
4. Carlson CB, Mowery P, Owen RM, Dykhuizen EC, Kiessling LL (2007) Selective tumor cell targeting using low-affinity, multivalent interactions. *ACS Chem Biol* 2:119–127.
5. Dobrucki LW, Sinusas AJ (2005) Molecular imaging — new approach to nuclear cardiology. *Q J Nucl Med Mol Imaging* 49:106–115.
6. Almutairi A, Guillaudeu SJ, Berezin MY, Achilefu S, Fréchet JMJ (2008) Biodegradable pH-sensing dendritic nanoprobes for near-infrared fluorescence lifetime and intensity imaging. *J Am Chem Soc* 130:444–445.
7. Gillies ER, Dy E, Fréchet JMJ, Szoka FC (2005) Biological evaluation of polyester dendrimer: Poly(ethylene oxide) ''bow-tie'' hybrids with tunable molecular weight and architecture. *Mol Pharmacol* 2:129–138.
8. Dijkgraaf I, *et al.* (2007) Synthesis of DOTA-conjugated multivalent cyclic-RGD peptide dendrimers via 1,3-dipolar cycloaddition and their biological evaluation: Implications for tumor targeting and tumor imaging purposes. *Org Biomol Chem* 5:935–944.
9. Weissleder R, Mahmood U (2001) Molecular imaging. *Radiology* 219:316–333.
10. Lee CC, MacKay JA, Fréchet JMJ, Szoka FC (2005) Designing dendrimers for biological applications. *Nat Biotechnol* 23:1517–1526.
11. Gillies ER, Fréchet JMJ (2005) Dendrimers and dendritic polymers in drug delivery. *Drug Discovery Today* 10:35–43.
12. Lee CC, *et al.* (2006) A single dose of doxorubicin-functionalized bow-tie dendrimer cures mice bearing C-26 colon carcinomas. *Proc Natl Acad Sci USA* 103:16649–16654.
13. De Jesus OLP, Ihre HR, Gagne L, Fréchet JMJ, Szoka FC (2002) Polyester dendritic systems for drug delivery applications: In vitro and in vivo evaluation. *Bioconjugate Chem* 13:453–461.
14. Adam MJ, Wilbur DS (2005) Radiohalogens for imaging and therapy. *Chem Soc Rev* 34:153–163.
15. Gillies ER, Fréchet JMJ (2002) Designing macromolecules for therapeutic applications: Polyester dendrimer-poly(ethylene oxide) ''bow-tie'' hybrids with tunable molecular weight and architecture. *J Am Chem Soc* 124:14137–14146.
16. Jeppesen C, *et al.* (2001) Impact of polymer tether length on multiple ligand-receptor bond formation. Science 293:465–468.
17. Yamada T, Kidera A (1996) Tailoring echistatin to possess higher affinity for integrin alpha(IIb)beta(3). *FEBS Lett* 387:11–15.
18. Zhang MR, Suzuki K (2007) F-18 fluoroalkyl agents: Synthesis, reactivity and application for development of PET ligands in molecular imaging. *Curr Top Med Chem* 7:1817–1828.
19. Sprague JE, *et al.* 2007) Noninvasive imaging of osteoclasts in parathyroid hormone-induced osteolysis using a Cu-64-labeled RGD peptide. *J Nucl Med* 48:311–318.
20. Romanov V, *et al.* (1997) Two novel probes reveal tubular and vascular Arg–Gly–Asp (RGD) binding sites in the ischemic rat kidney. *Kidney Int* 52:93–102.
21. Rossin R, Berndorff D, Friebe M, Dinkelborg LM, Welch MJ (2007) Small-animal PET of tumor angiogenesis using a Br-76-labeled human recombinant antibody fragment to the ED-B domain of fibronectin. *J Nucl Med* 48:1172–1179.
22. Guillaudeu SJ, *et al.* (2008) PEGylated dendrimers with core functionality for biological applications. *Bioconjugate Chem* 19:461–469.
23. Couffinhal T, *et al.* (1998) Mouse model of angiogenesis. *American Journal of Pathology* 152(6):1667–1679.
24. Hua J, *et al.* (2005) Noninvasive imaging of angiogenesis with a Tc-99m-labeled peptide targeted at alpha(v) beta(3) integrin after murine hindlimb ischemia. *Circulation* 111:3255–3260.